Granular Matter (2017) 19:77
DOI 10.1007/s10035-017-0766-x

ORIGINAL PAPER

A novel experimental device for investigating the multiscale behavior of granular materials under shear

Eloïse Marteau[1] · **José E. Andrade**[1]

Received: 16 May 2017 / Published online: 7 October 2017

Abstract In this paper, we report a set of experiments performed on a novel mechanical device that allows a specimen composed of a two-dimensional opaque granular assembly to be subjected to quasi-static shear conditions. A complete description of the grain-scale quantities that control the mechanical behavior of granular materials is extracted throughout the shear deformation. Geometrical arrangement, or fabric, is quantified by means of image processing, grain kinematics are obtained using Digital Image Correlation and contact forces are inferred using the Granular Element Method. Aiming to bridge the micro-macro divide, macroscopic average stresses for the granular assembly are calculated based on grain-scale fabric parameters and contact forces. The experimental procedure is detailed and validated using a simple uniaxial compression test. Macroscopic results of shear stress and volumetric strain exhibit typical features of the shear response of dense granular materials and indicate that critical state is achieved at large deformations. At the grain scale, attention is given to the evolution of fabric and contact forces as the granular assembly is sheared. The results show that shear deformation induces geometrical (fabric) and mechanical (force) anisotropy and that principal stresses and force orientation rotate simultaneously. At critical state, stress, force and fabric orientation reach the same value. By seamlessly connecting grain-scale information to continuum scale experiments, we shed light into the multiscale mechanical behavior of granular assemblies under shear loading.

✉ José E. Andrade
jandrade@caltech.edu

[1] Division of Engineering and Applied Science, California Institute of Technology, Pasadena, CA 91125, USA

Keywords Granular materials · Contact forces · Fabric · Multiscale · Critical state

1 Introduction

The macro-mechanical response of granular materials subjected to shear conditions has been extensively investigated by means of laboratory testing such as triaxial tests [1,2] and direct shear tests [3,4]. It is well-known that dense samples exhibit a peak in shear stress followed by a strain softening behavior, whereas in loose samples no peak is observed. However, at large shear deformation, both dense and loose samples show a tendency to stabilize around an asymptotic shear stress value that is uniquely related to the normal stress and void ratio. In term of volumetric deformations, dense samples initially contract and later dilate while loose samples only contract. For large shear strain values, the volumetric deformation of both systems reaches a constant value. This equilibrium state where no further changes in volume or stress state occur with increased shear deformation is conceptually defined as the critical state of a granular material. The critical state concept, first introduced by Casagrande [5] and considerably developed by Roscoe et al. [6], has provided a unifying approach to the fundamental understanding of the mechanical behavior of granular materials. The existence of a critical state has furnished a basis for the development of continuum constitutive models within the framework of plasticity theory [7–9]. Such models, known as the critical state soil mechanics framework, constitute one of the keystones of soil mechanics and have allowed practitioners to solve complex geomechanical engineering problems.

However, this modeling paradigm still has many limitations. Critical state plasticity models have been developed under the assumption that granular materials deform as

isotropic continua despite their discrete nature. Moreover, existing models have been derived from macroscopic observations obtained in the laboratory. Therefore, they heavily rely on the calibration of several state variables, which often lack a clear physical meaning. Phenomenological approaches also influence the predictive capabilities of most constitutive models when applied outside of their predetermined realm. As a consequence, there is currently a need to develop more physics-based constitutive models to better understand and accurately describe the continuum behavior of granular materials by embedding micromechanics. Significant efforts have been made in constructing multiscale analyses that provide a link between grain and continuum scale. Some of the most prominent examples include the stress-dilatancy theory, originally developed by Rowe [10], the stress-induced anisotropy [11–13], and the stress-strain-fabric relationship [14,15].

Many of these studies have been conducted using the discrete element method (DEM) [16] that has emerged as an important numerical technique to access grain-scale information such as contact forces and kinematics. In the recent past, DEM has been employed to micromechanically study the shear behavior of granular materials [17–20]. Nonetheless, DEM still has many limitations: it has a high computational cost, is generally constrained to simple grain shapes, and remains mainly qualitative.

Meanwhile, experimental testing remains an irreplaceable approach for investigating the fundamental response of granular materials. Shear tests performed on quasi-2D granular assemblies have proved their ability to provide key insights into the micromechanics of granular materials [21–25]. Such progress made in the field of experimental geomechanics are intimately linked to the development of grain-scale characterization techniques. In recent years, Digital Image Correlation (DIC) has been widely used to capture kinematics in granular assemblies [26–29]. By defining the best mapping function that relates two images, DIC provides full-field displacements, strains and rotation [30,31]. Force inference has been made possible by use of photoelasticity in assemblies of birefringent disks [13,32] and recently in assemblies of opaque, real granular materials in 2D [33–36] and 3D [37] by means of the Granular Element Method (GEM).

This paper presents an experimental capability that furnishes unique data on the mechanics of granular materials at different scales including continuum measures of stresses and strains and discrete measures of grain kinematics and contact forces. A key aspect of this experimental method is a novel apparatus allowing shear deformation at constant normal pressure of a 2D analogue granular assembly. At the grain scale, kinematics are extracted using DIC and normal and tangential contact forces are inferred with GEM, provided that average grain strains and contact point locations are known. We show that macroscopic results of stresses and strains reproduce typical features of the shear response of dense granular materials. To provide a validation process of the experimental method, we performed a uniaxial compression. This simpler loading condition gives us a direct comparison between applied load and results of normal stress computed from grain-scale quantities. In this study, we aim to improve our knowledge of the multiscale behavior of granular materials, which is essential for developing more physics-based constitutive models and for comparing laboratory tests with numerical simulations such as those performed with DEM.

For completeness, the paper is organized as follows. First, Sect. 2 presents the experimental setup and experimental procedure. Section 3 showcases a validation process of the experimental method. In Sect. 4, we give results that connect macroscopic stresses and strains with grain-scale information. Finally, Sect. 5 offers concluding remarks.

2 Experimental setup

2.1 Description of the apparatus

We have designed and built a novel experimental device capable of reproducing (quasi-static) simple shear conditions over large deformation on a two-dimensional analogue granular assembly. A general view of our apparatus is given in Fig. 1. In particular, Fig. 1a shows an exploded-view drawing of the device where the three main elements are showcased: (1) the support structure, (2) the shear cell, and (3) the linear actuator system. The support structure is made of a 1630 mm × 1270 mm 16 mm aluminum mounting plate and is directly placed onto a stationary steel table. Z-shaped members supporting the shear cell, L-shaped members supporting the glass plate, pulleys and y-axis linear guide rails are screwed to the aluminum plate. The shear cell consists of a horizontal deformable parallelogram (ABCD) that can undergo shear strain and normal strain in the y-direction (tilting and elongation of faces BC and AD). The points A and B are fixed to the Z-shaped members, themselves fixed to the support structure. The sides AB and CD are solid members that always remain horizontal and of constant length $L_x = 525$ mm while the lateral sides (BC and AD) consist of slotted members of variable length L_y. At the corners of the parallelogram ABCD, bearing arrangements mounted on rotary shafts allow the sides AD and BC to rotate at a constant angular velocity about the point A and the point B respectively. The shear angle γ between the vertical and the sides AD and BC can be positive or negative, allowing application of cyclic shear. The face CD of the shear cell remains parallel to the face AB and is mounted to the linear actuator system using bolted connections and a connector plate. The linear actuator system is composed of a brushless DC electric motor (MAXON Motor), belt drive, linear guide rails positioned in

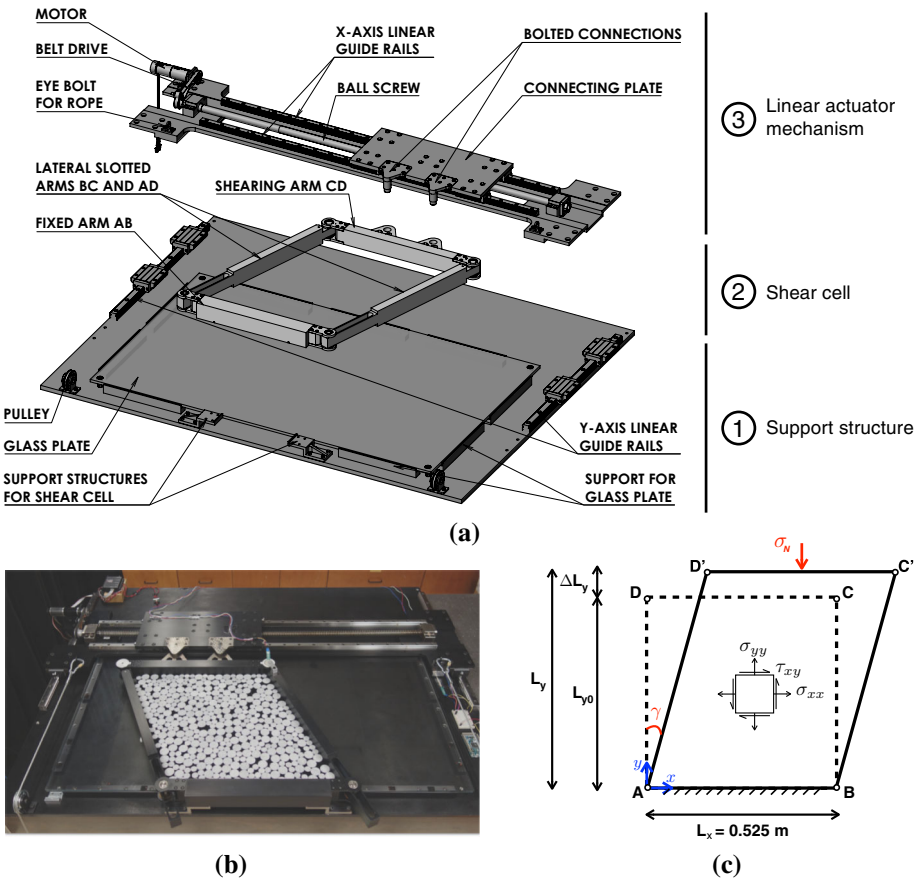

Fig. 1 Experimental shear apparatus. **a** Exploded view drawing. **b** Picture of the experimental setup. **c** Schematic depicting the state of deformation and imposed boundary conditions on the shear cell

the x-direction and a ball screw, mounted onto an aluminum x-drive plate. A linear motion in the x-direction is generated at the connector plate when the ball screw is rotated. This linear motion is transferred to the side CD of the shear cell and therefore provides the shear mechanism. Kinematic control of the shear mechanism is achieved by direct command of the speed of the DC motor using a speed controller (MAXON Motor) in a closed loop. Thus, during a test, the velocity of the side CD and the shear rate are kept constant. Furthermore, as shown in Fig. 1a, b, the linear actuator system is screwed on two y-axis linear guide rails fixed to the mounting plate. The y-axis linear guide mechanism enables movement of the linear actuator system in the y-direction and thus allows the faces BC and AD of the shear cell to elongate (or shorten). A constant normal stress σ_N is applied to the face CD of the shear cell and transmitted to the granular assembly using two pulley systems. On each side of the mounting plate, a hanging mass is suspended over a pulley while the other end of the rope is attached to the linear actuator system. Finally, the granular assembly stands on a glass plate and is tracked by an optical imaging system (Allied Vision Prosilica GT4907 15.7 Megapixel CCD camera attached to a Nikkor AF 105mm f/2.8 lens) that sits at 1.6 m above the apparatus. Image sequences are typically acquired at a frame rate of 7 images per second.

2.2 Measurements

Figure 1c displays the general state of deformation of the shear cell subjected to a prescribed tilting angle γ and external load σ_N. The angle γ between the vertical and the sides AD or BC and the length in the y-direction $L_y = L_{y0} + \Delta L_y$ constitute the two degrees of freedom that define the configuration of the shear cell. As illustrated in Fig. 1c, the length L_{y0} corresponds to the length of the sides AD and BC in the initial configuration (dashed lines) where the shear cell is a rectangle ($\gamma = 0$) and the length ΔL_y is the change in length in the y-direction. Measurements of the angle γ and the length L_y are performed using image processing. The limits on the dimensions of the shear cell are:

$$-35^\circ < \gamma < 35^\circ$$
$$450\ \text{mm} < L_y < 630\ \text{mm}$$

Given that the length in the x-direction is constant ($L_x = 525\,\text{mm}$), the component ϵ_{xx} of the strain tensor is equal to zero. Therefore, the macroscopic strain state is given by the following tensor:

$$\boldsymbol{\epsilon} = \begin{bmatrix} 0 & \epsilon_{xy} \\ \epsilon_{xy} & \epsilon_{yy}. \end{bmatrix}$$

where the normal strain $\epsilon_{yy} = \Delta L_y / L_y$ and the shear strain $\epsilon_{xy} = \tan\gamma/2$. Owing to the precise kinematic control of the shear mechanism, the macroscopic strain state is known at all time. The volumetric strain is defined as $\epsilon_v = \mathrm{tr}(\boldsymbol{\epsilon}) = \epsilon_{yy}$. Simple shear tests are performed in quasi-static conditions with a shear rate $\dot{\gamma} = 0.002\ \mathrm{s}^{-1}$. In two dimensions, the macroscopic stress state in the granular assembly is defined by the following tensor (see Fig. 1c):

$$\boldsymbol{\sigma} = \begin{bmatrix} \sigma_{xx} & \tau_{xy} \\ \tau_{xy} & \sigma_{yy} \end{bmatrix}$$

2.3 Material

We perform experiments on a two-dimensional analogue opaque granular assembly composed of 400 cylinders of height of 25 mm and of two different diameters, $d_1 = 20$ mm and $d_2 = 30$ mm. The grain diameters correspond to, respectively, 116 pixels and 172 pixels on the 4864 × 3232 pixels digital images captured at each time step. We emphasize that discs were used due to the simplicity of their manufacturing process. However, experiments can be carried out on arbitrary-shaped grains since the force inference method (GEM) does not make any assumption about grain shape [33,34]. The grains are made of polyurethane that has a Young's modulus E = 50 MPa, a Poissons ratio ν of approximately 0.5, and an inter-particle friction coefficient $\mu = 0.6$. For an optimal use of 2D-DIC, the top face of each cylinder is covered with suitable speckle patterns that are achieved by spraying black and white paints. Moreover, in order to minimize side and end friction between the shear cell and the granular assembly, PTFE dry lubricant is sprayed onto the aluminum members of the shear cell. We point out that, since the shear apparatus lays horizontally, the assembly preparation is not under gravity which does not influence the grain orientation and the force distributions.

3 Experimental method validation

To investigate the validity of the experimental capability presented in this paper, we performed a simple uniaxial compression test. In Sect. 3.1, we compare the results of macroscopic normal stress measured from the applied loads and the normal stress computed from grain-scale quantities, i.e. average grain stresses and contact forces. In Sect. 3.2, the contact forces inferred from GEM are used as input to compute an analytical stress contour distribution of $\sigma_1 - \sigma_2$ that is directly compared with measured 2D-DIC results.

3.1 Average macroscopic normal stress

A uniaxial compression test is carried out on the apparatus described in Sect. 2.1. In this test, the shear cell remains rectangular, such that the sides BC and AD can only elongate or shorten. It follows that the shear angle γ and the only non-zero component of the macroscopic strain tensor is $\epsilon_{yy} = \Delta L_y / L_y$. A normal stress σ_N is gradually applied to the granular assembly by linearly increasing the mass hanging over the pulley. The granular assembly is initially confined with a 20 lbs hanging mass, equal to an initial normal stress $\sigma_N^0 = -6.8$ kPa. At each load step, a 10 lbs weight is added, which corresponds to a normal stress increment of $\Delta\sigma_N = -3.4$ kPa. A sequence of images is collected with the image acquisition system detailed in Sect. 2.1 during the uniaxial compression test. Captured images are processed with image processing algorithm (i.e. Circular Hough Transform [38,39]) that perform circle detections from which the contact point locations are determined.

The 2D-DIC technique [30,31] is applied to the images to extract full-field displacement, strain and grain rotations. To perform this tracking, a correlation window (also called subset) of 15 × 15 pixels is chosen and a step size (i.e. the distance between neighboring calculation points) is set to 3 pixels. To determine an adequate correlation window size, one needs to find the tradeoff between spatial resolution and measurement error. The measurement error is evaluated by correlating two subsequent images of the specimen without applying any deformation. The values of the resulting strain components ($\epsilon_{xx}, \epsilon_{yy}$ and ϵ_{xy}) for different subset sizes are then compared in order to identify suitable configurations. With a 15 × 15 pixels correlation window, a border of 7 pixels around the edge of the grains are not correlated. However, since the force inference method (GEM) takes the average grain stresses as input [33,34], this data loss adjacent to the edges is not sufficient to compromise an accurate force calculation. Figure 2 shows the full-field strain distribution (ϵ_{xx}, ϵ_{yy} and ϵ_{xy}) obtained from 2D-DIC at the final load step where the granular assembly is subjected to a uniaxial compressive load of $\sigma_N = -54.4$ kPa (hanging mass of 160 lbs). The full-field stress distribution (σ_{xx}, σ_{yy} and σ_{xy}) is obtained by using the full-field strains in a linear elastic plane stress formulation. The corresponding principal stresses and are calculated at each pixel. Contour plot of difference of principal stresses are presented in Fig. 3 for the final load step ($\sigma_N = -54.4$ kPa, hanging mass of 160 lbs). The stress contour distribution gives us a direct comparison with stresses measured with photoelasticity [13,32,43]. Indeed, the isochromatic pattern obtained when a birefringent material is placed under stress is directly proportional to the difference of principal stresses $\sigma_1 - \sigma_2$ [40]. It can be seen from Figs. 2 and 3a that DIC measurements provide a qualitative information of the force distribution in an opaque granular assembly. Given that the position of the contact points and the average grain stress are known, force inference is performed with GEM [33,34]. GEM combines a mathematical framework with experimental data to infer

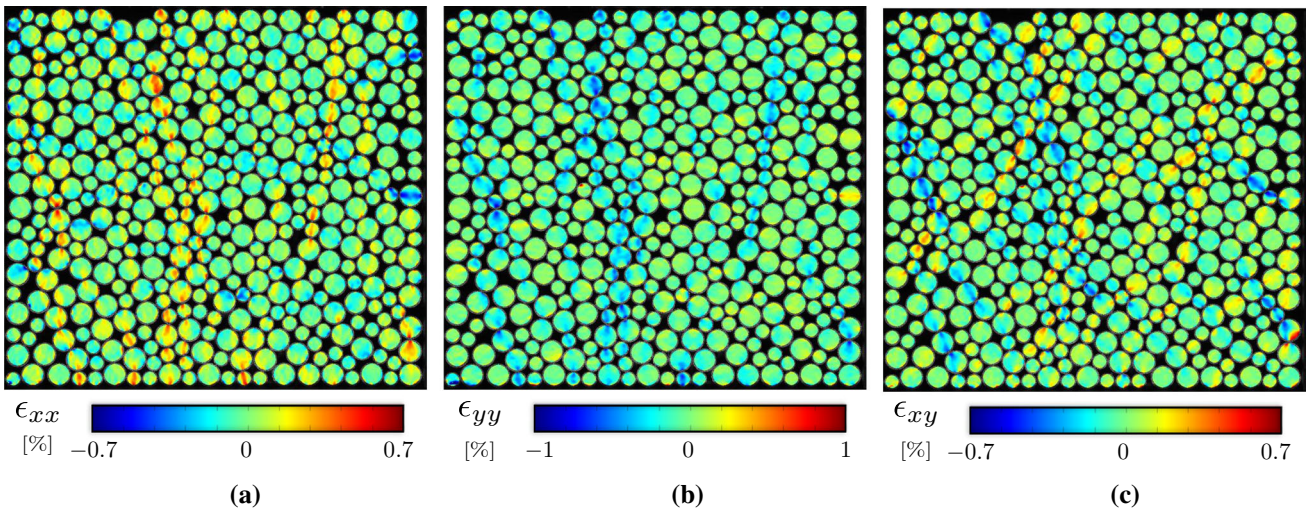

Fig. 2 Full-field strain measurements obtained using DIC during uniaxial compression test ($\gamma = 0$ and $\sigma_N = -54.4$ kPa). **a** Strain component ϵ_{xx}. **b** Strain component ϵ_{yy}. **c** Strain component ϵ_{xy}

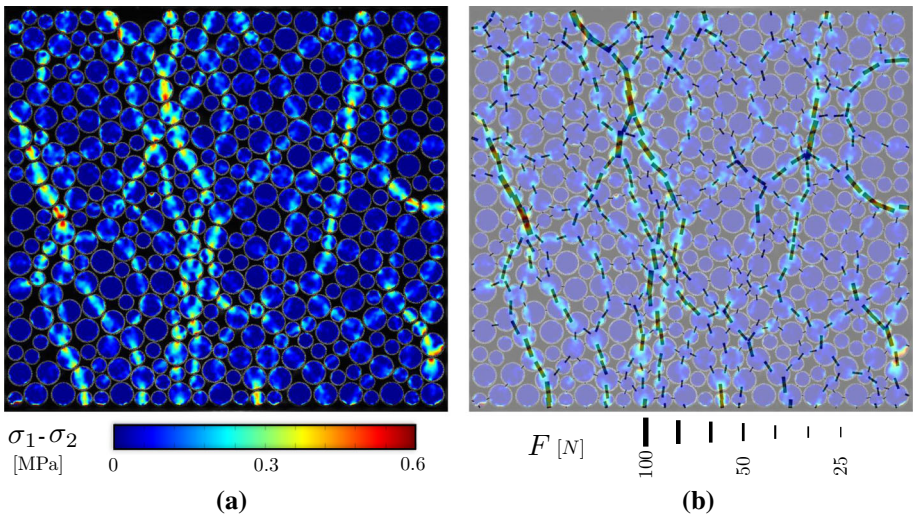

Fig. 3 **a** Contour distribution of difference in principal stresses $\sigma_1 - \sigma_2$. **b** Contact force magnitudes f obtained with GEM superimposed on contour distribution of difference in principal stresses $\sigma_1 - \sigma_2$

contact forces in granular assembly with grains of arbitrary shape, texture and opacity. The resulting contact forces for the uniaxial test are depicted in Fig. 3b. Figure 3b shows that the force magnitude matches really well measured stress contour distribution and that force chains are clearly seen to develop. GEM provides a quantitative assessment of force network.

The macroscopic stress response of the granular assembly subjected to external compressive loads is studied by incorporating grain-scale experimental information in two different ways. A first approach consists of computing the average Cauchy stress tensor $\bar{\boldsymbol{\sigma}}$ by simply taking the arithmetic mean of the average grain stresses $\bar{\boldsymbol{\sigma}}^p$, such that:

$$\bar{\boldsymbol{\sigma}} = \frac{1}{N_p} \sum_{p=1}^{N_p} \bar{\boldsymbol{\sigma}}^p \tag{1}$$

where N_p is the total number of grains. The average grain stresses $\bar{\boldsymbol{\sigma}}^p$ is obtained from average grain strains $\bar{\boldsymbol{\epsilon}}^p$ via $\bar{\boldsymbol{\sigma}}^p = \mathbb{C} : \bar{\boldsymbol{\epsilon}}^p$. Equation (1) links the DIC grain measurements with the macroscopic stress tensor $\bar{\boldsymbol{\sigma}}$. An alternative approach is to derive an expression for the average Cauchy stress tensor $\bar{\boldsymbol{\sigma}}$ in terms of fabric and contact forces and has been presented by Christoffersen et al. [41]:

$$\bar{\boldsymbol{\sigma}} = \frac{1}{\Omega} \sum_{\alpha=1}^{N_c} \mathrm{sym}(\boldsymbol{f}^\alpha \otimes \boldsymbol{d}^\alpha) \tag{2}$$

where N_c is the total number of contact points, Ω is the total volume of the granular assembly, $\boldsymbol{f}^\alpha$ is the contact force and $\boldsymbol{d}^\alpha$ is the branch vector at the contact α. The previous expression provides a relationship between the macroscopic stress tensor and the distribution of contact forces inferred with GEM. In Fig. 4a, we present results of average macroscopic

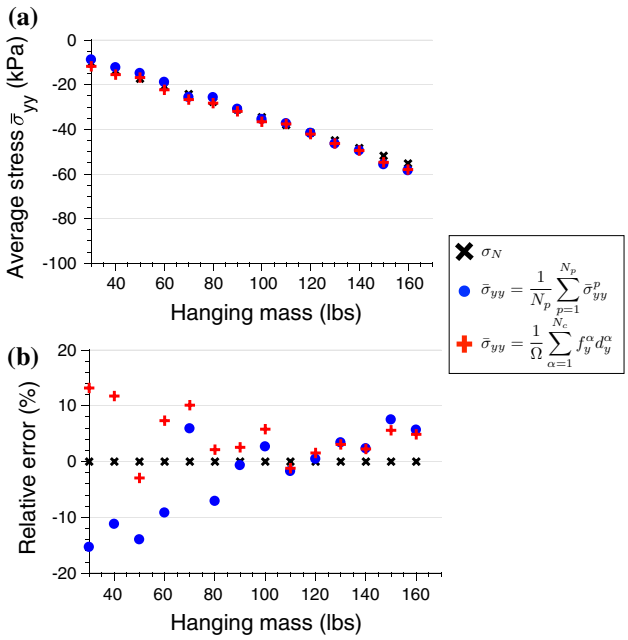

Fig. 4 **a** Comparison of applied normal stress σ_N with macroscopic average stress $\bar{\sigma}_{yy}$ inferred from DIC measurements and GEM results. **b** Relative error (in percent) between applied normal stress σ_N (black cross) and the measurements of macroscopic average stress $\bar{\sigma}_{yy}$ obtained from Eq. 1 (blue dots) and Eq. 2 (red plus sign) (color figure online)

stress in the y-direction $\bar{\sigma}_{yy}$ for the uniaxial compression test obtained from Eq. 1 (blue dots) and Eq. 2 (red plus sign) that are compared with the values of applied normal stress σ_N (black cross). Additionally, the relative error (in percent) between the applied normal stress σ_N and the measured average macroscopic stress $\bar{\sigma}_{yy}$ is presented in Fig. 4b. Potential error sources are versatile and include errors inherent to the optical measurement system, the mechanical device and the material property measurements, as well as intrinsic uncertainties of the DIC and GEM algorithms. Figure 4b demonstrates that the relative error remains below $\pm 15\%$ for all load steps and that measurements obtained from DIC (Eq. 1) does not yield more accurate results than those obtained from the micromechanics (Eq. 2). This comparison indicates that there is an excellent agreement between the macroscopic applied stress and stress measurements obtained from grain quantities. In other words, the stress state evaluated inside the granular assembly can reliably represent the stress measured at the boundary. These results give a direct link between macroscopic stress and evolution of fabric and contact forces and, therefore, between micro and macro scales.

3.2 Analytical stress contour distribution

By modeling the grains in the granular assembly as circular disks under in-plane loading, the stress distribution can be derived from an analytical solution based on the classical elasticity theory [42,43]. Analytical solution of stresses within a disk taken together with stress contour distribution visualized using photoelasticity techniques have been previously used to infer contact forces in birefringent granular material [13,32,44]. Grains used with photoelasticity in [13,44] are less stiff (Young's modulus E = 5 MPa) than the grains tested in this work (E = 50 MPa). However, both force inference methods, photoelasticity and GEM, can be used with materials of various stiffness as long as the optical imaging system has a sufficient spatial resolution to accurately detect deformation.

A detailed derivation of the analytical solution for a circular disk loaded by oblique concentrated forces at its boundary can be found in [45]. Hence, given the closed-form solution and knowing the value of the applied forces and the geometrical arrangement of the assembly (position of contact points), the analytical stress contour distribution within a disk is completely known. In this section, aiming to further validate our experimental procedure, we take the contact forces obtained from GEM as input to the analytical solution. In Fig. 5, the stress distribution derived from analytical formulations are compared with laboratory test results obtained from 2D-DIC where a uniaxial compression of -85 kPa is applied to the granular assembly. It can be seen from Fig. 5 that there is an excellent correlation between the patterns of principal stress contours as plotted from the analytical solutions and the contours observed with 2D-DIC. This grain to grain comparison gives us an indication of the accuracy of the magnitude and direction of the contact forces obtained with GEM.

4 Micro- to macroscopic response of granular materials under shear

Simple shear tests are carried out in order to characterize the micro- to macroscopic response of the granular assembly under shear. Each simple shear test begins by applying a constant normal stress σ_N to the granular assembly. We present here results of shear tests performed with three three different values of σ_N: $-$ 14.25, -28.5 and -42.75 kPa. The granular assembly is then sheared at a shear rate $\dot{\gamma} = 0.002\ \mathrm{s}^{-1}$. As in the uniaxial compression test, DIC measurements are performed to extract strain fields from which stress fields is deduced. MATLABs image processing toolbox is used to determined grain positions and contact locations for each acquired image so that the fabric evolution within the assembly is known at each time step. The contact forces are obtained by solving the GEM constrained optimization problem [33,34]. Figure 6 presents snapshots of the DIC results and contact forces distribution of the shear test performed at $\sigma_N = -28.5$ kPa for three different values of shear angle

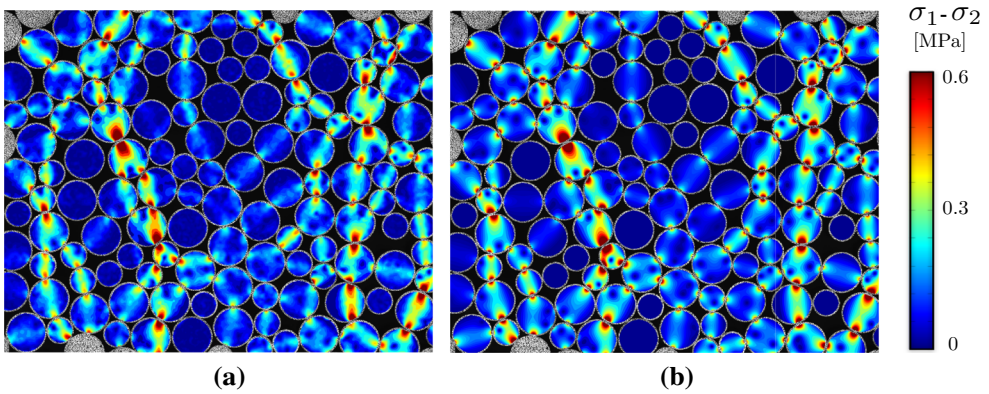

Fig. 5 Contour distribution of difference in principal stresses $\sigma_1 - \sigma_2$ **a** obtained from 2D-DIC **b** derived from analytical solutions

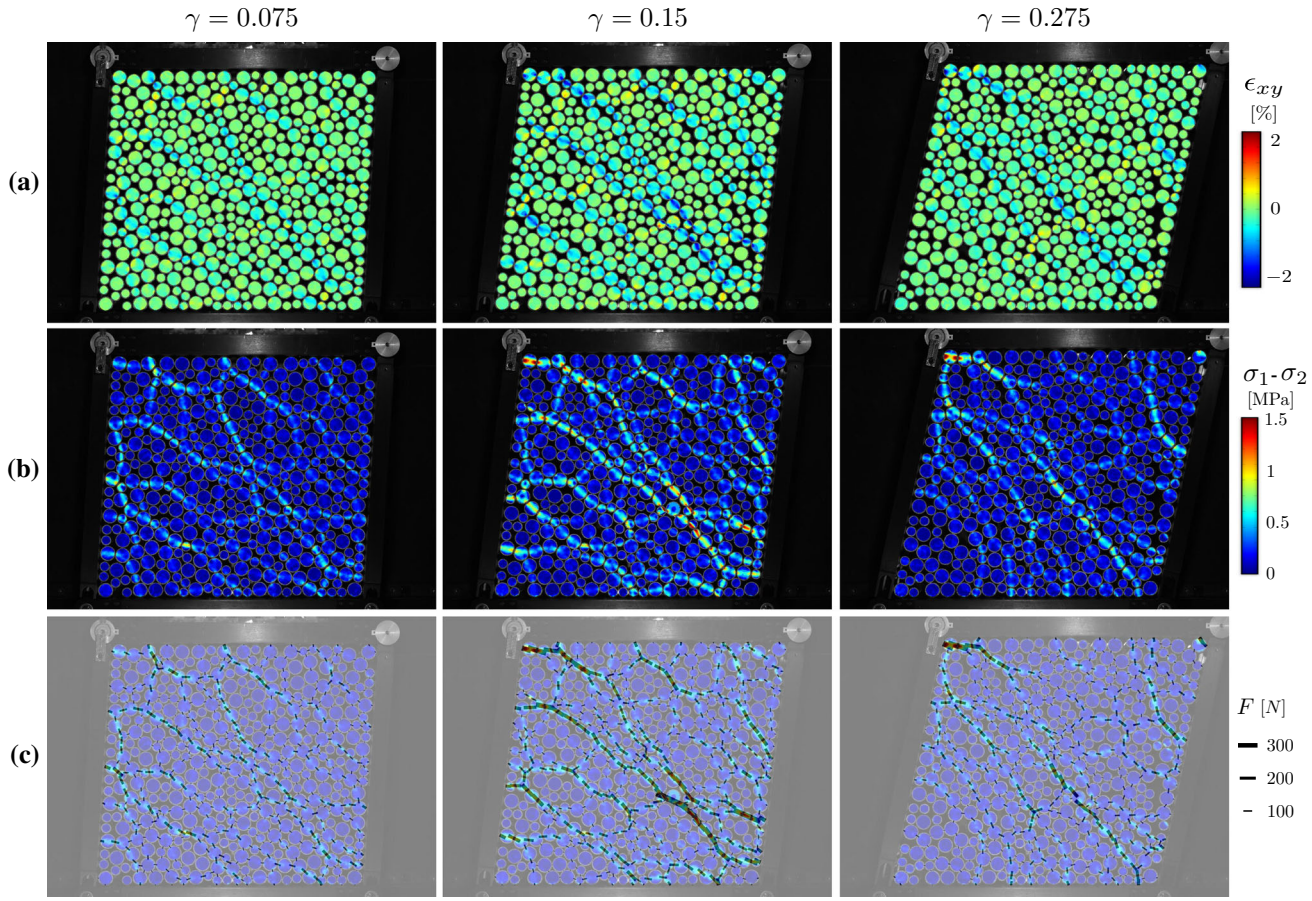

Fig. 6 Contour distribution of DIC measurements and GEM results for shear test ($\sigma_N = -28.5$ kPa) at $\gamma = 0.075$, 0.15 and 0.275. **a** Strain field ϵ_{xy}. **b** Difference of principal stresses $\sigma_1 - \sigma_2$. **c** Contact forces inferred with GEM superimposed on difference of principal stresses $\sigma_1 - \sigma_2$

($\gamma = 0.075$, 0.15 and 0.275). In Fig. 6, it can be seen that different force chain patterns form at different shear strain.

The macroscopic behavior of the granular assembly under shear is then investigated. First, macroscopic shear stress τ_{xy} is computed using Eq. 2 given the branch vector and contact force distributions. The results of such calculation for $\sigma_N = -14.25, -28.5$ and -42.75 kPa as a function of shear strain are shown in Fig. 7a. For all σ_N values, the granular material exhibits a linear elastic behavior followed by a peak in shear stress and subsequent strain softening. The observed stress-strain behavior is characteristic of a dense assembly subjected to shear deformation. In Fig. 7, vertical dashed lines indicate four distinct states of the shear behavior: (1) initial state ($\gamma = 0$); (2) linear elastic state ($\gamma = 0.075$); (3)

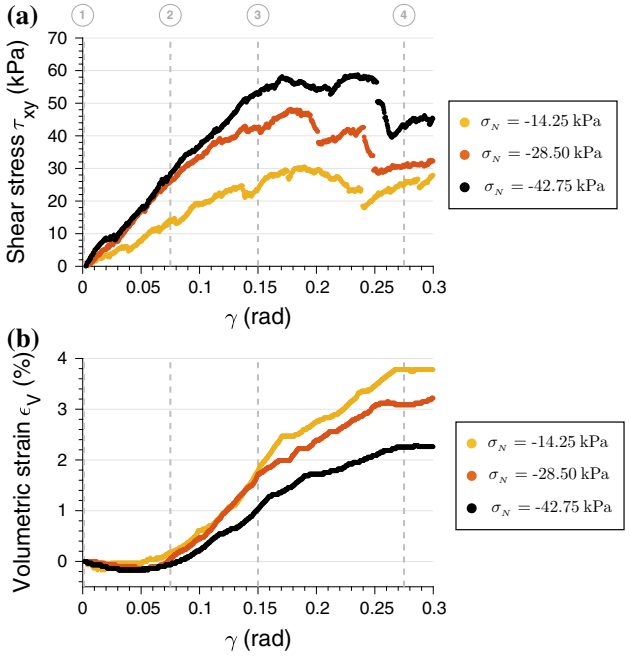

Fig. 7 Macroscopic behavior of the granular sample subjected to shear. **a** Shear stress τ_{xy} and **b** volumetric strain ϵ_V as a function of shear strain γ for applied normal stress $\sigma_N = -14.25$ KPa, -28.5 kPa and -42.75 kPa. Dashed vertical lines highlight four distinct states of the shear behavior: (1) initial state ($\gamma = 0$); (2) linear elastic state ($\gamma = 0.075$); (3) peak state ($\gamma = 0.15$); and (4) critical state ($\gamma = 0.275$)

peak state ($\gamma = 0.15$); and (4) critical state ($\gamma = 0.275$). It is worth noting that Fig. 6 shows snapshots of the granular assembly in linear elastic state ($\gamma = 0.075$), peak state ($\gamma = 0.15$) and critical state ($\gamma = 0.275$). In contrary to traditional laboratory experiments (such as triaxial and direct shear tests), our experimental procedure does not rely on boundary measurements of macroscopic stress obtained from load cells, which are typically used to study the constitutive behavior of granular materials [7–9]. As showcased by Eq. 2, micromechanical quantities involving branch vectors and contact forces are used as input to compute the macroscopic stresses. Such data incorporating micromechanics are generally not available in 3D experiments in which stress measurements are restricted to measurements at the boundary of the granular assembly. Volumetric versus shear strain curves obtained in experiments for three different value of applied normal stress σ_N are plotted in Fig. 7b. In Fig. 7b, we observe, once again, a typical behavior of a dense sample where the granular assembly initially contracts and then expands (dilates) until it reaches a constant volume at large shear deformation. The state in which the samples undergo large shear deformations without further changes in shear stress and volumetric strain corresponds to the critical state of the material. These results establish a link between grain-scale information, such as branch vectors and contact forces, and macroscopic laboratory observations.

The stress state of the granular assembly can also be visualized by looking at the magnitude of the normal stress $\sigma_A = \hat{\boldsymbol{n}}_A \cdot \bar{\boldsymbol{\sigma}} \cdot \hat{\boldsymbol{n}}_A$ acting on a plane of orientation θ, defined by the unit vector $\hat{\boldsymbol{n}}_A = (\cos\theta, \sin\theta)$. Starting from Equation (2), the magnitude of normal stress σ_A can be expressed in terms of the micromechanics as follow:

$$\sigma_A = \frac{1}{\Omega} \sum_{\alpha=1}^{N_c} f_A^\alpha d_A^\alpha \tag{3}$$

where f_A^α and d_A^α are the scalar projections of, respectively, the force vector and the branch vector at the contact α onto the unit vector $\hat{\boldsymbol{n}}_A$, i.e. $f_A^\alpha = \boldsymbol{f}^\alpha \cdot \hat{\boldsymbol{n}}_A$ and $d_A^\alpha = \boldsymbol{d}^\alpha \cdot \hat{\boldsymbol{n}}_A$. The polar representation of the normal stress σ_A for the shear test performed at $\sigma_N = -14.25$ kPa is shown in Fig. 8a. For each value of the angle $\theta \in [0, 2\pi]$, the magnitude of the normal stress $\sigma_A(\theta)$ is computed from the grain-scale quantities, i.e. the force vectors $\boldsymbol{f}^\alpha$ and the branch vectors $\boldsymbol{d}^\alpha$, according to Eq. 3. In this figure, σ_A is plotted for different values of shear angle γ that correspond to distinct states of the shear behavior: initial state ($\gamma = 0$, gray curve), linear elastic state ($\gamma = 0.075$, black curve), peak state ($\gamma = 0.15$, blue curve) and critical state ($\gamma = 0.275$, red curve). The polar representation of the normal stress σ_A given in Fig. 8a enables a clear visualization of the evolution of principal stress values (σ_1 and σ_2) and principal stress orientation, defined as the angle θ_p between the vertical axis and the major principal stress σ_1 axis. In the initial state ($\gamma = 0$), where the granular sample is subjected to uniaxial compression with $\sigma_N = -14.25$ kPa, we report that $\sigma_1 \approx \sigma_N$ and that the principal stress is oriented towards the vertical axis (direction of loading), such that $\theta_p = 0$. As the granular sample is sheared, the maximum principal stress value σ_1 increases until the peak and slightly decreases at critical state whereas the minimum principal stress value σ_2 only increases. Concurrently, as qualitatively reported in [23,46], Fig. 8a reveals that the principal stresses rotate clockwise (increase of θ_p) during shear. Figure 8b complements Fig. 8a as it depicts the evolution of the stress state (σ_{yy}, τ_{xy}) and (σ_{xx}, $-\tau_{xy}$) obtained from micromechanical quantities using Eq. 2 on a Mohr diagram (normal stress σ - shear stress τ plane). In this figure, stress states (colored circle markers) for the four distinct states (initial, linear elastic, peak and critical states) are highlighted and the corresponding Mohr circles are plotted. The stress state representation given in Fig. 8b shows stress continuity as the granular assembly is sheared. Initially, as $\gamma = 0$, the only stress applied to the granular assembly is a compressive stress in the vertical direction σ_N and the shear stress $\tau = 0$. It follows that the principal stresses $\sigma_1 = \sigma_{yy} \approx \sigma_N$ and $\sigma_2 = \sigma_{xx}$ (see Fig. 8b). As the shear angle γ increases, Fig. 8b shows that the stress components σ_{xx} and σ_{yy} increase until the peak state is reached. For

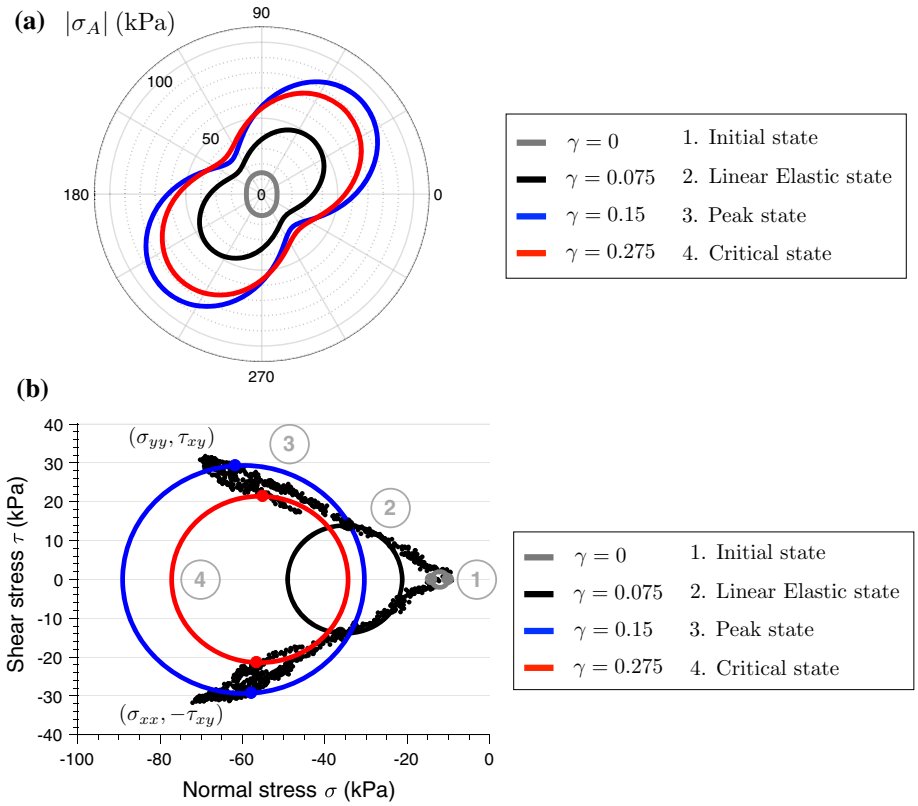

Fig. 8 **a** Polar distribution of normal stress σ_A in kPa for shear test ($\sigma_N = -14.25$ kPa) at $\gamma = 0, 0.075, 0.15$ and 0.275. σ_A is computed from grain-scale data (force and branch vectors) using Eq. 3. **b** Evolution of stress states (σ_{yy}, τ_{xy}) and $(\sigma_{xx}, -\tau_{xy})$ in kPa on a Mohr diagram (normal stress σ-shear stress τ plane). Mohr circles at $\gamma = 0, 0.075, 0.15$ and 0.275

a dense sample, we have seen that shear causes dilation. The top boundary of the shear cell (side CD) tends to obstruct this dilation from happening, such that the normal stress acting on the top boundary $\sigma_{CD} = \sigma_{yy}$ increases. Simultaneously, given the boundary conditions, an increase of σ_{yy} and τ_{xy} results in an increase of σ_{xx}. In particular, as the principal stress direction is rotated at an angle $\theta_p = 45°$ from the vertical axis, we have $\sigma_{xx} = \sigma_{yy}$. In this case, as showcased in Fig. 8b, the stress path presents a symmetry with respect to the $\tau = 0$ axis. Additionally, Mohr circle offers a useful graphical technique for finding principal stresses, i.e. in the plane where $\tau_{xy} = 0$. Comparison between the principal stress values obtained from the polar representation given in Fig. 8a and from the Mohr circles in Fig. 8b demonstrates the validity of Eq. 3 to compute principal stress values.

It can be seen from Eqs. 2 and 3 that the macroscopic stress tensor $\bar{\boldsymbol{\sigma}}$ and the magnitude of normal stress σ_A is linked to the contact forces and fabric. In order to gain a better understanding of the macroscopic behavior of granular materials during shear, it is therefore necessary to characterize the distribution of contact forces and contact orientations at the grain scale. We emphasize that for spherical grains, contact orientations are coincident with contact normal. Figure 9a shows a polar histogram of the probability density function (pdf) of contact orientations $P(\theta)$, i.e. number of contacts within an interval $\Delta\theta$ divided by the total number of contact N_c times $\Delta\theta$. Polar histograms of average normal forces $\bar{f}_n(\theta)$ and average tangential forces $\bar{f}_t(\theta)$ for different values of shear angle are depicted in Fig. 9b, c. Second order Fourier harmonic functions, as defined by [14,47], are used to approximate the polar distributions and are represented as dashed lines in Fig. 9. The polar histograms, shown in Fig. 9, confirm that shear stress applied to the granular assembly creates structural (fabric) anisotropy and mechanical (force) anisotropy.

From the grain-scale statistics and the Fourier expansions, we compute the angles θ_a and θ_f that correspond to the angles between the vertical axis and, respectively, the maximum value of contact orientation axis and the maximum value of average normal forces axis. In Fig. 10, principal stress orientation θ_p (black), contact orientation θ_a (green) and average normal force orientation θ_f (red) are plotted as a function of the shear strain γ. In this figure, the shaded markers represent the value of the different orientation angles θ obtained experimentally. The experimental data are then fitted using a smoothing spline [48]. The smoothed data is represented by the curves. Figure 10 shows that the rotation of principal stress occurs in the early stage of the shearing process; for $\gamma > 0.05$, the principal stress orientation θ_p remains nearly constant and $\theta_p \approx 45$? Throughout the shear deformation, principal stress orientation θ_p and average normal force orientation θ_f are coaxial. On the other hand, we experimentally demonstrate that the contact orientation θ_a does not generally coincide with the principal stress orienta-

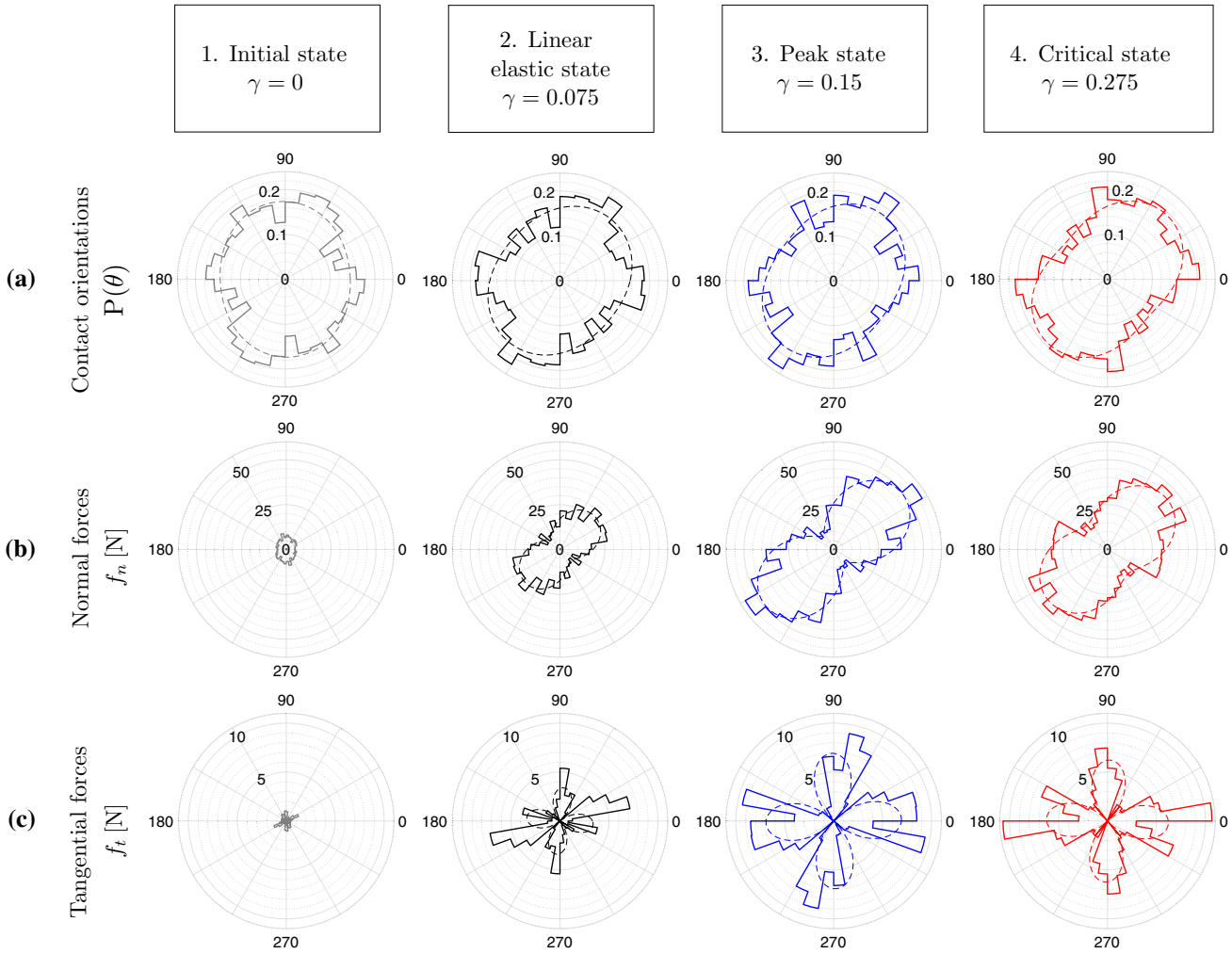

Fig. 9 Polar distribution for shear test ($\sigma_N = -14.25$ kPa) at $\gamma = 0$, 0.075, 0.15 and 0.275. **a** Probability density function of contact orientations P(θ). **b** Average normal forces $\bar{f}_n(\theta)$. **c** Average tangential forces $\bar{f}_t(\theta)$

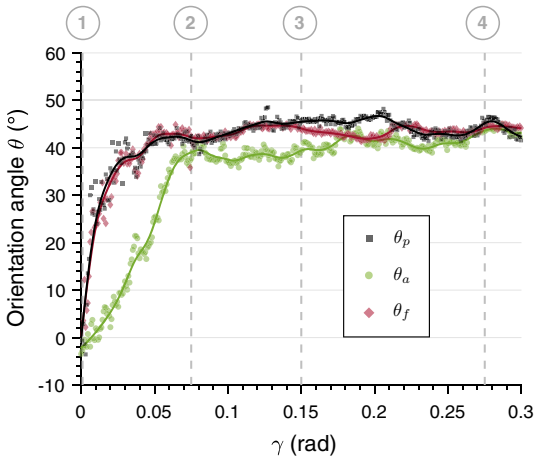

Fig. 10 Principal stress orientation (black), contact orientation (green) and average normal forces orientation (red) as a function of shear strain γ. The curves are obtained by smoothing the data (shaded markers) using a smoothing spline [48] (color figure online)

tion θ_p except once critical state is achieved ($\gamma > 0.225$) and at which $\theta_p \approx \theta_a \approx \theta_f$, as previously assumed in [14].

5 Closure

In this paper, we have described an experimental method that furnishes a complete description of the micro-mechanical state of granular materials: description of fabric (position of contact points and centroids), description of grain kinematics (displacements, rotations and strains) obtained using 2D-DIC and description of contact forces (normal and tangential components) obtained through GEM. We have introduced a novel experimental apparatus capable of reproducing the mechanical features of granular materials under shear loading. In particular, it has been shown that the so-called critical state is achieved at large shear strain. A uniaxial compres-

sion test was proposed as a benchmark test and has been successfully used to verify and validate the proposed experimental method. Under different loading conditions, force chains have been evidenced in an opaque granular assembly by means of 2D-DIC and quantified by GEM. We have connected macroscopic stresses to the microstructure through the evolution of fabric and contact forces. Principal stress, contact and average normal force orientations during shear have been studied and results show coaxiality between principal stress and average normal forces orientations while contact orientation is lagging behind until critical state is reached. These results may serve as a validation of DEM simulations and enhance our understanding of the multiscale behavior of granular materials.

Acknowledgements This work was supported in part by the Defense Threat Reduction Agency (DTRA) under award number HDTRA1-12-1-0041. This support is gratefully acknowledged.

Compliance with ethical standards

Conflict of interest No potential conflict of interest is reported by the authors. None of the material presented in the paper is submitted or published elsewhere, and the paper does not contain any information with restricted access or proprietary content.

Appendix: The granular element method

In this appendix, we describe the GEM algorithm in a pseudo-code format. Let i_p and i_α denote the storage indices for, respectively, the p-th particle and the α-th contact, for $\alpha \in \{1, \ldots, N_c\}$ and $p \in \{1, \ldots, N_p\}$. N_p is the total number of grains and N_c is the total number of contact. For more details on the mathematical framework of GEM, see [33–35].

Inputs:
Position of contact points $\boldsymbol{x} = [\boldsymbol{x}^1, \boldsymbol{x}^2, \ldots, \boldsymbol{x}^{N_c}]^T$ where $\boldsymbol{x}^\alpha = \{x^\alpha, y^\alpha\}$
Average grain stress $\bar{\boldsymbol{\sigma}} = [\bar{\boldsymbol{\sigma}}^1, \bar{\boldsymbol{\sigma}}^2, \ldots, \bar{\boldsymbol{\sigma}}^{N_p}]^T$ where $\bar{\boldsymbol{\sigma}}^p = \{\bar{\sigma}^p_{xx}, \bar{\sigma}^p_{yy}, \bar{\sigma}^p_{xy}\}$
Surface of grains $\Omega = [\Omega_1, \Omega_2, \ldots, \Omega_{N_p}]^T$
Normal unit contact vector $\boldsymbol{e} = [\boldsymbol{e}^1, \boldsymbol{e}^2, \ldots, \boldsymbol{e}^{N_c}]^T$ where $\boldsymbol{e}^\alpha = \{e^\alpha_x, e^\alpha_y\}$
Tangential unit contact vector $\boldsymbol{t} = [\boldsymbol{t}^1, \boldsymbol{t}^2, \ldots, \boldsymbol{t}^{N_c}]^T$ where $\boldsymbol{t}^\alpha = \{t^\alpha_x, t^\alpha_y\}$
Inter-particle friction coefficient μ
Boundary of granular assembly Γ

Output:
Force vector $\boldsymbol{f} = [\boldsymbol{f}^1, \boldsymbol{f}^2, \ldots, \boldsymbol{f}^{N_c}]^T$ where $\boldsymbol{f}^\alpha = \{f^\alpha_x, f^\alpha_y\}$

Algorithm 1 The Granular Element Method (GEM)

Initialize
Construct vector $\boldsymbol{b}_{st} = [\boldsymbol{b}^1_{st}, \boldsymbol{b}^2_{st}, \ldots, \boldsymbol{b}^{N_p}_{st}]^T$
for p = 1 to N_p **do**
  Compute $\boldsymbol{b}^p_{st} = \{\Omega_p \bar{\sigma}^p_{xx}, \Omega_p \bar{\sigma}^p_{yy}, 2\Omega_p \bar{\sigma}^p_{xy}\}$
  Assemble $\boldsymbol{b}_{st}(i_p) = \boldsymbol{b}^p_{st}$
end for
Construct matrices $\boldsymbol{K}_{eq}$, $\boldsymbol{K}_{st}$ and $\boldsymbol{B}$
for α = 1 to N_c **do**
  Identify master grain p
  Compute $\boldsymbol{K}^\alpha_{eq} = [\{1, 0\}, \{0, 1\}, \{y^\alpha, -x^\alpha\}]$
  Assemble $\boldsymbol{K}_{eq}(i_p, i_\alpha) = \boldsymbol{K}^\alpha_{eq}$
  Compute $\boldsymbol{K}^\alpha_{st} = [\{x^\alpha, 0\}, \{0, y^\alpha\}, \{x^\alpha, y^\alpha\}]$
  Assemble $\boldsymbol{K}_{st}(i_p, i_\alpha) = \boldsymbol{K}^\alpha_{st}$
  if $\alpha \notin \Gamma$ **then**
    Identify slave grain q
    Assemble $\boldsymbol{K}_{eq}(i_q, i_\alpha) = -\boldsymbol{K}^\alpha_{eq}$
    Assemble $\boldsymbol{K}_{st}(i_q, i_\alpha) = -\boldsymbol{K}^\alpha_{st}$
  end if
  Compute $\boldsymbol{B}_1(\alpha, i_\alpha) = [-e^\alpha_x, -e^\alpha_y]$
  Compute $\boldsymbol{B}_2(\alpha, i_\alpha) = [-e^\alpha_x - t^\alpha_x/\mu, -e^\alpha_y - t^\alpha_y/\mu]$
  Compute $\boldsymbol{B}_3(\alpha, i_\alpha) = [-e^\alpha_x + t^\alpha_x/\mu, -e^\alpha_y + t^\alpha_y/\mu]$
  Assemble $\boldsymbol{B} = [\boldsymbol{B}_1, \boldsymbol{B}_2, \boldsymbol{B}_3]^T$
end for
Solve optimization problem
for $\lambda \in [0, 1]$ **do**
  Minimize $(\lambda||\boldsymbol{K}_{eq}\boldsymbol{f}|| + (1-\lambda)||\boldsymbol{K}_{st}\boldsymbol{f} - \boldsymbol{b}_{st}||)$ with respect to $\boldsymbol{f}$ subjected to $\boldsymbol{B}\boldsymbol{f} \geq 0$
  Store $||\boldsymbol{K}_{eq}\boldsymbol{f}||$, $||\boldsymbol{K}_{st}\boldsymbol{f} - \boldsymbol{b}_{st}||$ and $\boldsymbol{f}$
end for
Find the preferred solution $\boldsymbol{f}^*$ corresponding to the knee point of the $(||\boldsymbol{K}_{eq}\boldsymbol{f}||, ||\boldsymbol{K}_{st}\boldsymbol{f} - \boldsymbol{b}_{st}||)$ curve
Return $\boldsymbol{f} = \boldsymbol{f}^*$

References

1. Bardet, J.-P.: Experimental Soil Mechanics. Prentice Hall, Upper Saddle River (1997)
2. Bishop, A.W., Henkel, D.J.: The Measurement of Soil Properties in the Triaxial Test. Hodder Arnold H&S, London (1970)
3. Kjellman, W.: Testing the shear strength of clay in Sweden. Gotechnique **2**, 225–232 (1951)
4. Roscoe, K.H.: An apparatus for the application of simple shear to soil samples. In: Proceedings of 3rd International Conference on Soil Mechanics Foundation Engineering, Zurich, pp. 186–191 (1953)
5. Casagrande, A.: Characteristics of cohesionless soils affecting the stability of slopes and earth fills. J. Boston Soc. Civil Eng. (1936)
6. Roscoe, K.H., Schofield, A.N., Wroth, C.P.: On the yielding of soils. Gotechnique **8**, 22–53 (1958)
7. Schofield, A.N., Wroth, P.: Critical State Soil Mechanics. McGraw-Hill Book Co., London (1968)
8. Parry, R.H.G.: Stress–Strain Behavior of Soils. G.T. Foulis and Co., Henley (1972)
9. Muir Wood, D.: Soil Behavior and Critical State Soil Mechanics. Cambridge University Press, Cambridge (1990)
10. Rowe, P.W.: The stress-dilatancy relation for static equilibrium of an assembly of particle in contact. Proc R. Soc. A **269**, 500–527 (1962)
11. Oda, M., Nemat-Nasser, S., Konishi, J.: Stress-induced anisotropy in granular masses. Soils Found. **25**, 85–97 (1985)

12. Thornton, C.: Induced anisotropy and energy dissipation in particulate material—results from computer-simulated experiments. In: Yielding, Damage, and Failure of Anisotropic Solids. Mechanical Engineering Publications, London, pp. 113–130 (1990)
13. Majmudar, T.S., Behringer, R.P.: Contact force measurements and stress-induced anisotropy in granular materials. Nature **435**, 1079–1082 (2005)
14. Rothenburg, L., Bathurst, R.J.: Analytical study of induced anisotropy in idealized granular materials. Geotechnique **39**, 601–614 (1989)
15. Ouadfel, H., Rothenburg, L.: Stress–force–fabric relationship for assemblies of ellipsoids. Mech. Mater. **33**, 201–221 (2001)
16. Cundall, P.A., Strack, O.D.L.: A discrete numerical model for granular assemblies. Gotechnique **29**, 47–65 (1979)
17. Masson, S., Martinez, J.: Micromechanical analysis of the shear behavior of a granular material. J. Eng. Mech. **127**, 1007–1016 (2001)
18. Thornton, C.: Numerical simulations of deviatoric shear deformation of granular media. Gotechnique **50**, 43–53 (2000)
19. Cui, L., O'Sullivan, C.: Exploring the macro- and micro-scale response of an idealised granular material in the direct shear apparatus. Gotechnique **56**, 455–468 (2006)
20. Fu, P., Dafalias, Y.F.: Fabric evolution within shear bands of granular materials and its relation to critical state theory. Int. J. Numer. Anal. Methods Geomech. **35**, 1918–1948 (2011)
21. Calvetti, F., Combe, G., Lanier, J.: Experimental micromechanical analysis of a 2D granular material: relation between structure evolution and loading path. Mech. Cohesive Frict. Mater. **2**, 121–163 (1997)
22. Matsuoka, H.: A microscopic study of shear mechanism of granular materials. Soils Found. **14**, 29–43 (1974)
23. Oda, M., Konishi, J.: Rotation of principal stresses in granular material during simple shear. Soils Found. **14**, 39–53 (1974)
24. Oda, M., Konishi, J.: Microscopic deformation mechanism of granular material in simple shear. Soils Found. **14**, 25–38 (1974)
25. Howell, D., Behringer, R.P.: Stress fluctuations in a 2D granular Couette experiment: a continuous transition. Phys. Rev. Lett. **82**, 5241 (1999)
26. Hall, S.A., Desrues, J., Viggiani, G., Besuelle, P., Ando, E.: Experimental characterisation of (localised) deformation phenomena in granular geomaterials from sample down to inter- and intra-grain scales. Procedia IUTAM **4**, 54–65 (2012)
27. Hall, S., Wood, D.M., Ibraim, E., Viggiani, G.: Localised deformation patterning in 2D granular materials revealed by digital image correlation. Granul. Matter **12**, 1–14 (2009)
28. Vitone, C., Viggiani, G., Cotecchia, F., Hall, S.A.: Localized deformation in intensively fissured clays studied by 2D digital image correlation. Acta Geotech. **8**, 247–263 (2013)
29. Rechenmacher, A.L.: Grain-scale processes governing shear band initiation and evolution in sands. J. Mech. Phys. Solids **63**, 154–166 (2005)
30. Pan, B., Qian, K., Xie, H., Asundi, A.: Robust full-field measurement considering rotation using digital image correlation. Meas. Sci. Technol. **20**, 062001 (2009)
31. Sutton, M.A., Orteu, J.J., Schreier, H.: Image Correlation for Shape, Motion and Deformation Measurements: Basic Concepts, Theory and Applications. Springer, USA (2009)
32. Drescher, A.: Photoelastic verification of a mechanical model for the flow of a granular material. J. Mech. Phys. Solids **20**, 337–340 (1972)
33. Andrade, J.E., Avila, C.F.: Granular element method (GEM): linking inter-particle forces with macroscopic loading. Granul. Matter **14**, 51–61 (2012)
34. Hurley, R.C., Marteau, E., Ravichandran, G., Andrade, J.E.: Extracting inter-particle forces in opaque granular materials: beyond photoelasticity. J. Mech. Phys. Solids **63**, 154–166 (2014)
35. Hurley, R.C., Lim, K.W., Ravichandran, G., Andrade, J.E.: Dynamic inter-particle force inference in granular materials: method and application. Exp. Mech. **56**, 217–229 (2016)
36. Karanjgaokar, N.: Evaluation of energy contributions using inter-particle forces in granular materials under impact loading. Granul. Matter **19**, 36 (2017)
37. Hurley, R.C., Hall, S.A., Andrade, J.E., Wright, J.: Quantifying interparticle forces and heterogeneity in 3D granular materials. Phys. Rev. Lett. **117**, 098005 (2016)
38. Ballard, D.H.: Generalizing the Hough transform to detect arbitrary shapes. Pattern Recognit. **13**, 111–122 (1981)
39. Peng, T.: Detect circles with various radii in grayscale image via hough transform. http://www.mathworks.com/matlabcentral/fileexchange (2010)
40. Doyle, J.F.: Manual on experimental stress analysis. Society for Experimental Mechanics (1989)
41. Christoffersen, J., Mehrabadi, M.M., Nemat-Nasser, S.: A micromechanical description of granular material behavior. J. Appl. Mech. **48**, 339–344 (1981)
42. Timoshenko, S., Goodier, J.N.: Theory of Elasticity. McGraw-Hill Book Co, New York (1951)
43. Frocht, M.M.: Photoelasticity. Wiley, New York (1941)
44. Daniels, K.E., Kollmer, J.E., Puckett, J.G.: Photoelastic force measurements in granular materials. https://arxiv.org/abs/1612.03525 (2016)
45. Surendra, K.V.N., Simha, K.R.Y.: Characterizing frictional contact loading via isochromatics. Exp. Mech. **54**, 1011–1030 (2014)
46. Roscoe, K.H., Bassett, R.H., Cole, E.R.L.: Principal axes observed during simple shear of a sand. In: Proceedings of Geotechnical Conference, Oslo, pp. 231–237 (1967)
47. Radjai, F., Wolf, D.E., Jean, M., Moreau, J.J.: Bimodal character of stress transmission in granular packing. Phys. Rev. Lett. **80**, 61–64 (1998)
48. Reinsch, C.H.: Smoothing by spline functions. Numer. Math. **10**, 177–183 (1967)